Elastic least-squares reverse time migration

Yuting Duan, Paul Sava, and Antoine Guitton, Center for Wave Phenomena, Colorado School of Mines*

SUMMARY

Least-squares migration (LSM) can produce images with improved resolution and reduced migration artifacts. We propose a method for elastic least-squares reverse time migration (LSRTM) based on a new perturbation imaging condition that yields scalar images of squared P and S velocity perturbations. These perturbation images are simply related to physical subsurface properties, and in addition, they do not suffer from polarity reversals seen with other more conventional elastic imaging methods. We use 2D examples to demonstrate the proposed LSRTM algorithm using our perturbation imaging condition. Results show that elastic LSRTM increases the image resolution and attenuates artifacts, while providing images where the relative amplitudes of the reflectors can be used for reservoir characterization.

INTRODUCTION

Advances in seismic acquisition and ongoing improvements in computational capability make imaging using elastic waves increasingly feasible (Sun et al., 2006; Yan and Sava, 2008; Denli and Huang, 2008; Artman et al., 2009; Wu et al., 2010; Du et al., 2012; Duan and Sava, 2015; Rocha et al., 2015). Compared to acoustic images, elastic images can provide more information about the subsurface, e.g., fracture distributions and elastic properties. However, elastic migration also suffers from issues that negatively affect the quality of the images. Because it is in general difficult to separate all arrivals in the recorded data by wave mode, some arrivals are migrated using an incorrect velocity model. Such nonphysical modes lead to artifacts (i.e. cross-talk) in the image (Duan et al., 2014).

Least-squares migration (LSM) is an improved imaging algorithm that reduces these migration artifacts and also improves the resolution of migration images. LSM is a linearized waveform inversion that seeks to find the image that best predicts, in a least-squares sense, the recorded seismic data (Schuster, 1993; Nemeth et al., 1999; Dai et al., 2011). Schuster (1993) proposes LSM for cross-well data while Nemeth et al. (1999) apply this technique to surface data. Their studies show that LSM can significantly improve the spatial resolution of the images, and can also reduce migration artifacts arising from limited aperture, coarse sampling, and acquisition gaps.

LSM can be implemented using a Kirchhoff engine (Nemeth et al., 1999; Dai et al., 2011), one-way wave equation (Kuehl et al., 2002; Kaplan et al., 2010; Huang and Schuster, 2012), or two-way wave equation, i.e., least squares reverse-time migration (LSRTM) (Dai and Schuster, 2013; Dong et al., 2012; Luo and Hale, 2014; Wong et al., 2015). Although computationally expensive, RTM is advantageous for velocity models with complicated geologic structures that result in wavefield multipathing.

A key component for elastic LSRTM is the imaging condition, and many different types of imaging conditions for elastic media have been proposed. For example, Yan and Sava (2008) propose a displacement imaging condition that crosscorrelates each component of source and receiver displacement wavefields. They also propose a potential imaging condition that crosscorrelates P- and S-wave modes in source and receiver wavefields. One issue with this potential imaging condition is that the image components for converted waves change polarity at normal incidence. Stanton and Sacchi (2015) use a LSRTM method based on this imaging condition, including an additional polarity correction in the angle domain. Duan and Sava (2015) propose a scalar imaging condition for converted waves that produces scalar images without polarity reversal; however, this imaging condition requires knowledge of the geologic dip.

In this paper we propose an elastic LSRTM method based on a new perturbation imaging condition, which we derive for squared P and S velocities. Images computed using this new imaging condition can be simply related to physical subsurface properties, and in addition, these images do not suffer from polarity changes and thus can be stacked over experiments without an additional polarity correction. Using the perturbation imaging condition, we demonstrate that we obtain elastic LSRTM images with higher resolution and less migration artifacts than RTM.

THEORY

LSM aims to find the image that best predicts, in a least-squares sense, the recorded seismic data. For elastic migration, we consider a vector image $\mathbf{m}$ which contains both compressional and shear wave information. Migration is an adjoint operator $\mathbf{F}^{\mathsf{T}}$ that maps recorded data $\mathbf{d}$ to an image $\mathbf{m}$, and corresponding linearized forward process can be expressed as

$$\mathbf{F}\mathbf{m} = \mathbf{d}\,, \tag{1}$$

where $\mathbf{F}$ is the demigration operator.

LSM updates the model iteratively by minimizing the objective function

$$J(\mathbf{m}) = \sum_e \frac{1}{2} \|\mathbf{D}\left(\mathbf{F}\mathbf{m} - \mathbf{d}_r\right)\|^2\,, \tag{2}$$

which evaluates the misfit between observed data $\mathbf{d}_r(e,\mathbf{x},t)$ and predicted data $\mathbf{F}\mathbf{m}$ for each experiment e. Matrix $\mathbf{D}(e,\mathbf{x},t)$ denotes a data weighting operator, which can be applied for various purposes. For example, Trad et al. (2015) use matrix $\mathbf{D}$ to eliminate the impact of high-amplitude noise or missing traces on inversion; Wong et al. (2015) use matrix $\mathbf{D}$ to down-weight salt reflection energy. In this paper, we use the data weighting term to balance the amplitudes of the recorded data.

Perturbation models are derived using the Born approximation (Hudson and Heritage, 1981; Jaramillo and Bleistein, 1999;

Ribodetti et al., 2011). We consider the homogeneous elastic isotropic wave-equation:

$$\ddot{\mathbf{u}}_s - \alpha\nabla(\nabla\cdot\mathbf{u}_s) + \beta\nabla\times(\nabla\times\mathbf{u}_s) = \mathbf{d}_s\ , \tag{3}$$

where $\mathbf{u}_s(e,\mathbf{x},t) = [u_x \quad u_y \quad u_z]^T$ is the source displacement wavefield, which is a function of experiment e, space $\mathbf{x}$, and time t. Vector $\mathbf{d}_s(e,\mathbf{x},t)$ is the source function. Parameters $\alpha(\mathbf{x}) = \dfrac{\lambda+2\mu}{\rho}$ and $\beta(\mathbf{x}) = \dfrac{\mu}{\rho}$ are squared P- and S-wave velocities, respectively. λ and μ are the Lamé parameters, and ρ is the density.

The perturbation $\mathbf{m} = \left[I^\alpha \quad I^\beta\right]^T$ to the background model gives the perturbed model $\left[\alpha + I^\alpha \quad \beta + I^\beta\right]^T$. The total wavefield $\mathbf{u}_s + \delta\mathbf{u}_s$ is computed using the same source term $\mathbf{d}_s$:

$$\begin{aligned}(\ddot{\mathbf{u}}_s + \delta\ddot{\mathbf{u}}_s) - (\alpha + I^\alpha)\nabla[\nabla\cdot(\mathbf{u}_s+\delta\mathbf{u}_s)] \\ + \left(\beta + I^\beta\right)\nabla\times[\nabla\times(\mathbf{u}_s+\delta\mathbf{u}_s)] = \mathbf{d}_s\ ,\end{aligned} \tag{4}$$

where $\delta\mathbf{u}_s$ is the perturbed wavefield:

By ignoring higher order terms $I^\alpha\nabla(\nabla\cdot\delta\mathbf{u}_s)$ and $I^\beta\nabla\times(\nabla\times\delta\mathbf{u}_s)$, and subtracting equation 3 from equation 4, we obtain a relation for the perturbed wavefield $\delta\mathbf{u}_s$:

$$\begin{aligned}&\delta\ddot{\mathbf{u}}_s - \alpha\nabla(\nabla\cdot\delta\mathbf{u}_s) + \beta\nabla\times(\nabla\times\delta\mathbf{u}_s) \\ &= [\nabla(\nabla\cdot\mathbf{u}_s) \quad -\nabla\times(\nabla\times\mathbf{u}_s)]\begin{bmatrix}I^\alpha \\ I^\beta\end{bmatrix}\ .\end{aligned} \tag{5}$$

The predicted data are extracted from the perturbed wavefield $\delta\mathbf{u}_s$ at the receiver locations.

We define a matrix $\mathbf{W}$ that, at each time and space position, is given by

$$\mathbf{W} = [\nabla(\nabla\cdot\mathbf{u}_s) \quad -\nabla\times(\nabla\times\mathbf{u}_s)]\ . \tag{6}$$

In this matrix, the first and second elements are the decomposed P- and S-modes of the source wavefield $\mathbf{u}_s$, respectively. The demigration operator in equation 1 thus becomes

$$\mathbf{F} = \mathbf{KPW}\ , \tag{7}$$

where $\mathbf{P}$ represents an elastic forward modeling operator that computes the perturbed wavefield $\delta\mathbf{u}_s$ for a source term $\mathbf{Wm}$; $\mathbf{K}$ is an operator that restricts the perturbed wavefield $\delta\mathbf{u}_s$ to the known receiver positions. Equation 7 maps the image $\mathbf{m}$ to the data $\mathbf{d}_r$, and its adjoint operator

$$\mathbf{F}^\mathsf{T} = \mathbf{W}^\mathsf{T}\mathbf{P}^\mathsf{T}\mathbf{K}^\mathsf{T}\ . \tag{8}$$

maps the data $\mathbf{d}_r$ to the image $\mathbf{m}$; the operator $\mathbf{K}^\mathsf{T}$ injects the recorded data $\mathbf{d}_r$ into the wavefield, and the adjoint wave propagation operator $\mathbf{P}^\mathsf{T}$ computes the receiver displacement wavefield $\mathbf{u}_r = \mathbf{P}^\mathsf{T}\mathbf{K}^\mathsf{T}\mathbf{d}_r$. Equation 8 describes a perturbation imaging condition for elastic RTM, because the application of the adjoint operator $\mathbf{F}^\mathsf{T}$ to the recorded data $\mathbf{d}_r$ yields the images

$$I^\alpha = \sum_{e,t}\nabla(\nabla\cdot\mathbf{u}_s)\cdot\mathbf{u}_r, \tag{9}$$

$$I^\beta = \sum_{e,t} -\nabla\times(\nabla\times\mathbf{u}_s)\cdot\mathbf{u}_r\ , \tag{10}$$

for the α and β models, respectively. From equation 8, we see that images I^α and I^β are computed by taking the zero-lag crosscorrelation of elements of the matrix $\mathbf{W}$ with the displacement receiver wavefield $\mathbf{u}_r$. These perturbation images do not suffer from polarity reversal, which is a common issue for elastic images whose values are related to angle-dependent reflectivities.

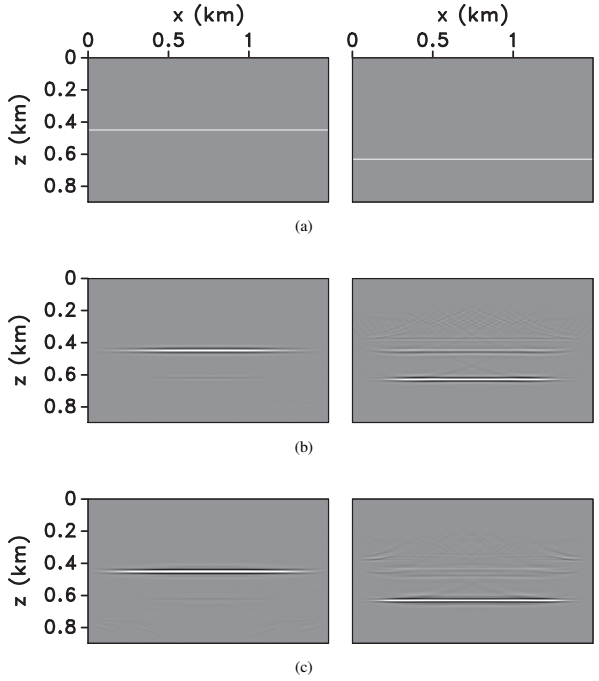

Figure 1: (a) Synthetic experiment with α (left) and β (right) models depicting reflectors at different depths. Inverted α (left) and β (right) models after (b) 1 and (c) 10 iteration(s) of elastic LSRTM.

EXAMPLES

We use two examples to demonstrate our method for elastic migration. The first example is layered and each of the α and β models contains one horizontal reflector at different depths, as shown in Figure 1a. We generate 30 two-component shot gathers using a vertical displacement source with a 30 Hz peak frequency Ricker wavelet. Using the perturbation imaging condition (equation 7), we obtain the images for α and β shown in Figure 1b. Notice that additional reflectors appear in both α and β images; these reflectors are generated by unphysical modes in the constructed receiver wavefield. Figures 1c show the LSRTM images after 10 iterations. Compared to the images shown in Figure 1b, the LSRTM images have higher resolution and contain fewer artifacts.

We also demonstrate our method with a modified version of the Marmousi-II model (Martin et al., 2006). This model is fully elastic, and supports not only compressional waves, but also shear waves and converted waves. The model simulates hydrocarbon reservoirs that dramatically decrease the value of α,

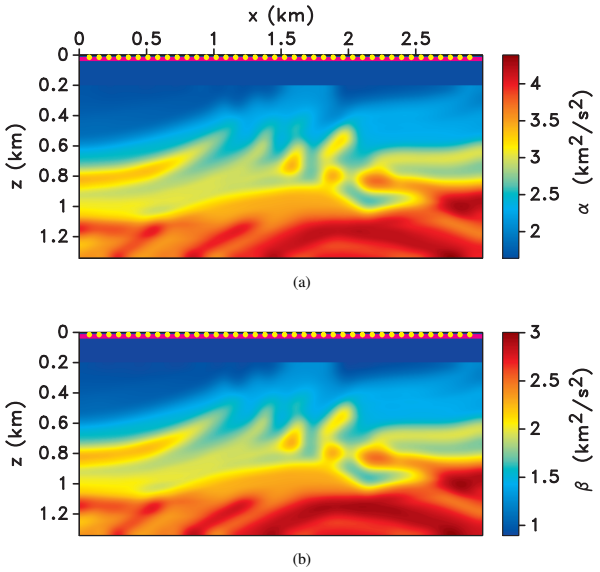

Figure 2: Background (a) α and (b) β models for the Marmousi example. The line at $z = 0.025$ km represents the receivers, and the dots at $z = 0.013$ km denote the locations of the sources. The top layer is homogeneous for both background models.

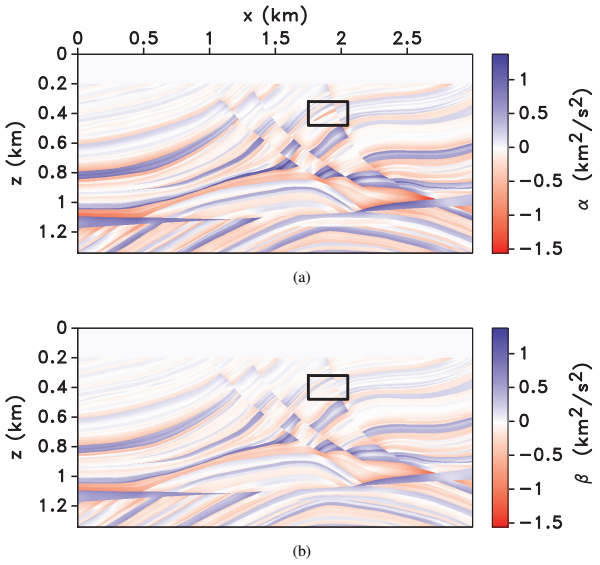

Figure 3: Marmousi example depicting (a) α and (b) β perturbation models. The models are not identical, e.g., the reservoir with negative value in the highlighted area is present only in the α model.

but slightly increase the value of β. Figures 2a and 2b show the background α and β models, respectively; both model contain a homogeneous layer at the top. Figures 3a and 3b show the corresponding true perturbation models for α and β, respectively, which are inconsistent in reservoir areas, for example, the highlighted box in Figures 3a and 3b. This inconsistency poses a challenge for elastic LSRTM, e.g. if the inversion allows a leakage between model parameters.

We model 40 shots evenly spaced on the surface using a displacement source with a 30 Hz peak frequency Ricker wavelet. The horizontal and vertical components of the source function have the same amplitudes in order to generate strong shear waves. The receiver spread is fixed for all shots and spans from 0 to 3.0 km with a 5 m sampling.

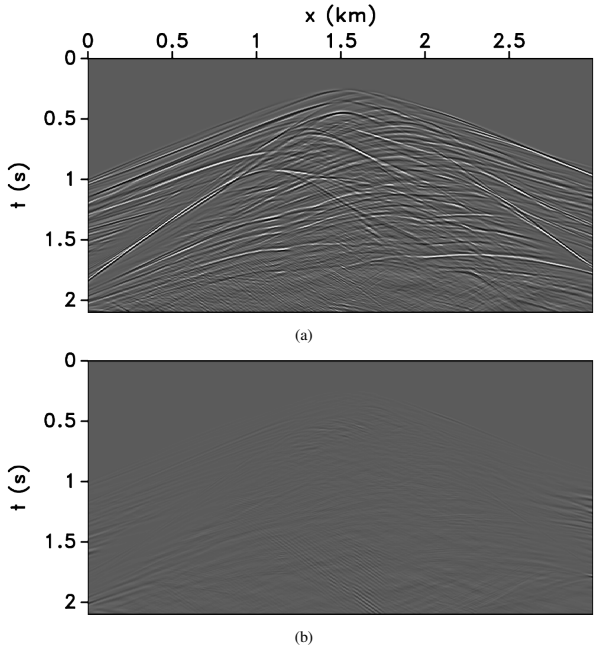

Figure 4: Horizontal component of the weighted (a) shot gather, and (b) the data residual after 112 iterations.

The recorded data are modeled according to equation 8. In order to obtain a uniform update using all arrivals, we use the data weighting term **D** to balance the arrivals with weak amplitudes. We define the data weighting function based on the inverse of the data envelope. Figures 4a is the horizontal component of the weighted recorded shot gather, demonstrating that the amplitudes of all arrivals are well balanced.

Figures 5a and 5b show the RTM images for α and β, respectively. We observe that the events for the shallow reflectors in both models have stronger amplitudes compared to those of the deeper reflectors, and strong backscattering is present due to the sharp interfaces in the background model. We apply an illumination compensation based on the source wavefield $\mathbf{u}_s$ to the RTM images and LSRTM gradients, in order to balance nonuniform data coverage.

The LSRTM images after 112 iterations, where the conver-

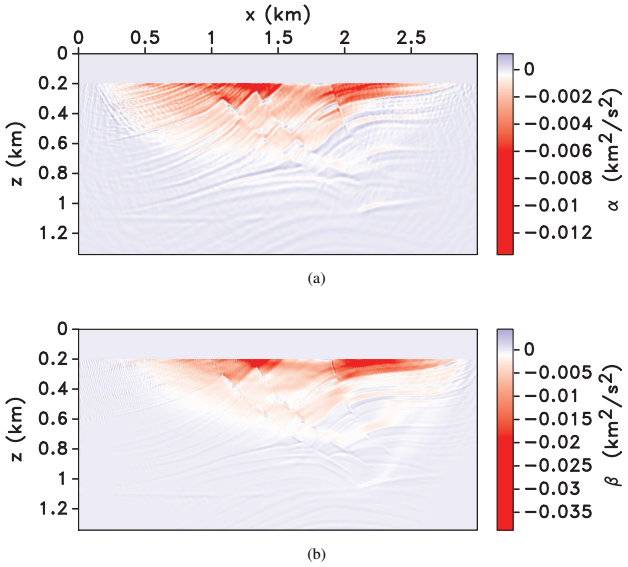

Figure 5: RTM (a) α and (b) β images with illumination compensation based on the source wavefield.

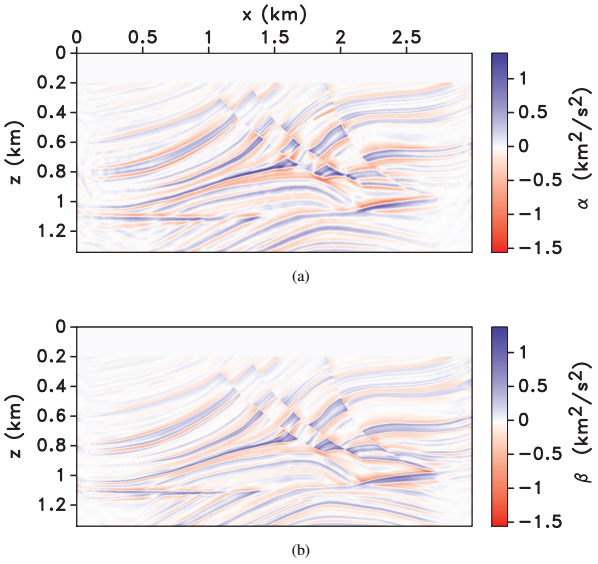

Figure 6: Updated (a) α and (b) β images after 112 iterations. Note that the reservoir near coordinates $\{1.9, 0.4\}$ km is correctly recovered in the updated α image, without any leakage in the updated β image.

gence curve becomes flat, are shown in Figures 6a and 6b. The update image for α has higher resolution than β because, in general, S waves have shorter wavelengths than P waves, and we do not consider attenuation in this experiment. The updated images are consistent with the true perturbation images. For example, only the α image (Figure 6a) contains the reflector with negative value highlighted in Figure 3a, which corresponds to a hydrocarbon reservoir in the true model that decreases the value of α.

Figures 4b shows the horizontal component of the data residual after 112 iterations. The amplitudes of all arrivals in the data residual after inversion are small, i.e., for most arrivals, the predicted data match the recorded data in both phase and amplitude. Figures 7a and 7b compare traces from the inverted α and β images at $x = 1.5$ km with the true perturbation models. Because we use Born data generated using the same wave equation as the recorded data, the amplitudes of the LSRTM images match well the true perturbation models. In practice, with errors in the background models and approximations of the wave equation, we may not obtain true-amplitude LSRTM images; however, the relative amplitudes of the reflectors can still be estimated correctly, which is beneficial for reservoir characterization.

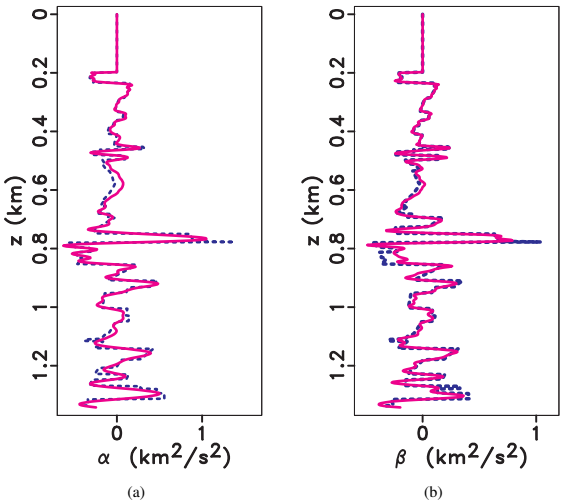

Figure 7: Comparison between inverted images (solid lines) and true perturbation images (dashed lines) for (a) α and (b) β models.

CONCLUSIONS

We propose a method for elastic least-squares reverse time migration using a perturbation imaging condition. The images computed using our method represent perturbations of squared P and S velocities. Compared to RTM, LSRTM has higher computational cost, and more work is needed to improve its convergence rate. Nevertheless, elastic LSRTM produces high-resolution images that provide correct relative amplitudes, which makes our algorithm especially suitable for applications such as reservoir characterization.

ACKNOWLEDGMENTS

We thank the sponsors of the Center for Wave Phenomena, whose support made this research possible. The reproducible numeric examples in this paper use the Madagascar open-source software package (Fomel et al., 2013) freely available from http://www.ahay.org.

REFERENCES

Artman, B., I. Podladtchikov, and A. Goertz, 2009, Elastic time-reverse modeling imaging conditions: SEG Technical Program Expanded Abstracts 2009, 1207–1211.

Dai, W., and G. T. Schuster, 2013, Plane-wave least-squares reverse-time migration: Geophysics, **78**, S165–S177.

Dai, W., X. Wang, and G. T. Schuster, 2011, Least-squares migration of multisource data with a deblurring filter: Geophysics, **76**, R135–R146.

Denli, H., and L. Huang, 2008, Elastic-wave reverse-time migration with a wavefield-separation imaging condition: SEG Technical Program Expanded Abstracts 2008, 2346–2350.

Dong, S., J. Cai, M. Guo, S. Suh, Z. Zhang, B. Wang, Z. Li, et al., 2012, Least-squares reverse time migration: towards true amplitude imaging and improving the resolution: Presented at the 2012 SEG Annual Meeting, Society of Exploration Geophysicists.

Du, Q., Y. Zhu, and J. Ba, 2012, Polarity reversal correction for elastic reverse time migration: Geophysics, **77(2)**, S31–S41.

Duan, Y., and P. Sava, 2015, Scalar imaging condition for elastic reverse time migration: Geophysics, **80**, S127–S136.

Duan, Y., P. Sava, et al., 2014, Elastic reverse-time migration with OBS multiples: Presented at the 2014 SEG Annual Meeting, Society of Exploration Geophysicists.

Fomel, S., P. Sava, I. Vlad, Y. Liu, and V. Bashkardin, 2013, Madagascar: open-source software project for multidimensional data analysis and reproducible computational experiments: Journal of Open Research Software, **1**, e8.

Huang, Y., and G. T. Schuster, 2012, Multisource least-squares migration of marine streamer and land data with frequency-division encoding: Geophysical Prospecting, **60**, 663–680.

Hudson, J., and J. Heritage, 1981, The use of the Born approximation in seismic scattering problems: Geophysical Journal International, **66**, 221–240.

Jaramillo, H. H., and N. Bleistein, 1999, The link of Kirchhoff migration and demigration to Kirchhoff and Born modeling: Geophysics, **64**, 1793–1805.

Kaplan, S. T., P. S. Routh, and M. D. Sacchi, 2010, Derivation of forward and adjoint operators for least-squares shot-profile split-step migration: Geophysics, **75**, S225–S235.

Kuehl, H., M. Sacchi, et al., 2002, Robust AVP estimation using least-squares wave-equation migration: Presented at the 2002 SEG Annual Meeting, Society of Exploration Geophysicists.

Luo, S., and D. Hale, 2014, Least-squares migration in the presence of velocity errors: Geophysics, **79**, S153–S161.

Martin, G. S., R. Wiley, and K. J. Marfurt, 2006, Marmousi2: An elastic upgrade for Marmousi: The Leading Edge, **25**, 156–166.

Nemeth, T., C. Wu, and G. T. Schuster, 1999, Least-squares migration of incomplete reflection data: Geophysics, **64**, 208–221.

Ribodetti, A., S. Operto, W. Agudelo, J.-Y. Collot, and J. Virieux, 2011, Joint ray+ Born least-squares migration and simulated annealing optimization for target-oriented quantitative seismic imaging: Geophysics, **76**, R23–R42.

Rocha, D., N. Tanushev, P. Sava, et al., 2015, Elastic wavefield imaging using the energy norm: Presented at the 2015 SEG Annual Meeting, Society of Exploration Geophysicists.

Schuster, G. T., 1993, Least-squares cross-well migration: SEG Technical Program Expanded Abstracts, 110–113.

Stanton, A., and M. Sacchi, 2015, Least squares wave equation migration of elastic data: Presented at the 77th EAGE Conference and Exhibition 2015.

Sun, R., G. A. McMechan, C. Lee, J. Chow, and C. Chen, 2006, Prestack scalar reverse-time depth migration of 3D elastic seismic data: Geophysics, **71(5)**, S199–S207.

Trad, D., et al., 2015, Least squares Kirchhoff depth migration: implementation, challenges, and opportunities: Presented at the 2015 SEG Annual Meeting, Society of Exploration Geophysicists.

Wong, M., B. L. Biondi, and S. Ronen, 2015, Imaging with primaries and free-surface multiples by joint least-squares reverse time migration: Geophysics, **80**, S223–S235.

Wu, R., R. Yan, and X, 2010, Elastic converted-wave path migration for subsalt imaging: SEG Technical Program Expanded Abstracts 2010, 3176–3180.

Yan, J., and P. Sava, 2008, Isotropic angle-domain elastic reverse-time migration: Geophysics, **73(6)**, S229–S239.